

Two-and-a-half Order Score-based Model for Solving 3D Ill-posed Inverse Problems

Zirong Li, Yanyang Wang, Jianjia Zhang and Weiwen Wu, Hengyong Yu, *Senior Member, IEEE*

Abstract—Computed Tomography (CT) and Magnetic Resonance Imaging (MRI) are crucial technologies in the field of medical imaging. Score-based models have proven to be effective in addressing different inverse problems encountered in CT and MRI, such as sparse-view CT and fast MRI reconstruction. However, these models face challenges in achieving accurate three dimensional (3D) volumetric reconstruction. The existing score-based models primarily focus on reconstructing two dimensional (2D) data distribution, leading to inconsistencies between adjacent slices in the reconstructed 3D volumetric images. To overcome this limitation, we propose a novel two-and-a-half order score-based model (TOSM). During the training phase, our TOSM learns data distributions in 2D space, which reduces the complexity of training compared to directly working on 3D volumes. However, in the reconstruction phase, the TOSM updates the data distribution in 3D space, utilizing complementary scores along three directions (sagittal, coronal, and transaxial) to achieve a more precise reconstruction. The development of TOSM is built on robust theoretical principles, ensuring its reliability and efficacy. Through extensive experimentation on large-scale sparse-view CT and fast MRI datasets, our method demonstrates remarkable advancements and attains state-of-the-art results in solving 3D ill-posed inverse problems. Notably, the proposed TOSM effectively addresses the inter-slice inconsistency issue, resulting in high-quality 3D volumetric reconstruction.

Index Terms—Image Reconstruction, 3D Inverse Problems, Score-based Model, Computed Tomography, Magnetic Resonance Imaging.

I. INTRODUCTION

OVER the years, Computed Tomography (CT) and Magnetic Resonance Imaging (MRI) have become cornerstones in modern clinical diagnosis [1]. Particularly, sparse-view CT [2] and fast MRI techniques [3] rapidly achieve superior image quality with shorter scanning time [4]. Sparse-view CT imaging usually reduces the number of scanning views and increases the view intervals to minimize radiation dose and scanning time. Similarly, fast MRI techniques aim to reduce the amount of measured data in k-space for faster scans [5]. While these advancements have shown promising

results, they are a new set of ill-posed inverse problems that need to be effectively addressed [6].

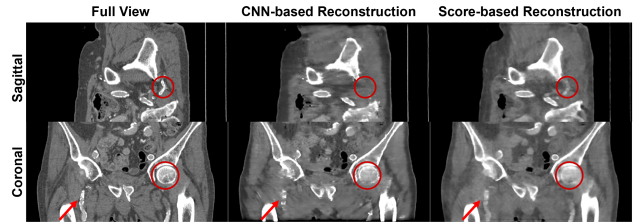


Fig. 1. The reconstructed CT images from 29 views reveal noticeable inter-slice inconsistency in the sagittal and coronal planes when both the CNN-based and score-based reconstruction methods are employed.

Deep learning-based methods have been developed to improve the reconstruction quality from individual slices within 2D space. These methods include convolution neural networks (CNNs) [7], generative adversarial networks (GANs) [8], and more recent transformer techniques [9]. Very recently, the score-based models have emerged as a promising alternative approach to solve ill-posed inverse problems and achieved excellent results [10] [11]. These models focus on learning the underlying data distribution and estimating the corresponding gradients. By leveraging this gradient information, the score-based models can generate high-quality reconstructions from limited data or noisy measurements [12].

However, most of these methods focus on reconstructing 2D image slices. Although these methods have demonstrated significant advancements, one usually acquires high-fidelity 3D volumetric images of sparse-view CT and fast MRI reconstruction [13]. When it comes to 3D volumetric reconstruction (see Fig. 1), the existing score-based models face a challenge known as inter-slice inconsistency [6]. This issue arises when independently reconstructed 2D slices are stacked to form a 3D volume [14], resulting in inconsistencies and artifacts, particularly in the sagittal and coronal planes. This phenomenon hinders accurate and cohesive reconstruction of 3D volumetric images, which is crucial in clinical applications.

The fundamental issue of the inter-slice inconsistency lies in the insufficient learning and modeling of the 3D data distribution in the score-based models [15]. While 2D score-based models have demonstrated proficiency in capturing data distribution within 2D contexts, their limited capacity prevents them from extending this comprehension to cover the entire 3D volume. As a result, the inter-slice relationships and correlations, which are necessary for achieving a cohesive and

Z. Li, Y. Wang J. Zhang and W. Wu are with the Department of Biomedical Engineering, Sun-Yat-sen University, Shenzhen Campus, Shenzhen, China. H. Yu is with the Department of Electrical and Computer Engineering, University of Massachusetts Lowell, Lowell, MA, USA. This study is supported in part by the National Natural Science Foundation of China (No: 62201628).

Z. Li and Y. Wang contributed equally. Corresponding authors are W. Wu (wuweiw7@mail.sysu.edu.cn) and H. Yu (hengyong-yu@ieee.org).

precise 3D reconstruction, are not fully utilized [16]. Indeed, it poses several challenges to train 3D score-based models for reconstruction tasks. First, the utilization of such a model in medical imaging demands substantial GPU resources to process 3D volumes. Second, it is a highly intricate process to train a 3D data distribution, often yielding suboptimal scores and consequently leading to suboptimal reconstructions.

To address the issue of inter-slice inconsistency, the state-of-the-art methods incorporate additional prior information to capture inter-slice relationships. For example, one introduces the regularization of L_1 total variation (TV) [17] in the z-axis direction, aiming at addressing the issue of discontinuities between slices [6]. Another method pre-trains two orthogonal score-based models to obtain inter-slice information [18]. However, both of the aforementioned methods have limitations. First, they do not fully model the distribution of the 3D data or perform score updates on 3D volumes. Second, they introduce excessive regularization terms, making it challenging to balance multiple hyper-parameters. Additionally, it doubles the computational cost to pre-train two models in the latter method, limiting its practical deployment.

To overcome the limitations in existing methods, an ideal score-based model for 3D reconstruction should accurately model the distribution of 3D data. Moreover, to release the computational burden associated with 3D scoring networks, the reconstruction method should estimate the 3D distribution using a pre-trained 2D score-based model. This can leverage the knowledge acquired from the transaxial plane, enabling higher computational efficiency for reconstruction while still benefiting from a comprehensive understanding of the 3D data distribution. Furthermore, to avoid introducing excessive hyper-parameters for fast convergence and lower complexity, a 2D score-based model can be trained without additional regularization constraints to compute the 3D score. This can simplify the training process and enhance the practicality and implementation of the reconstruction method in practice.

Based on the aforementioned analysis, this paper presents a method called two-and-a-half (2.5) order score-based model (TOSM) to address the inter-slice inconsistency and leverage advanced score-based models for high-quality 3D reconstruction from under-sampled data. The key concept of TOSM is based on the knowledge that the data distribution within each plane of the same volumetric image is similar. By training a 2D score-based model to learn the data distribution in the transaxial plane, we can utilize this model to calculate scores along the transaxial, sagittal, and coronal planes, resulting in three pseudo-3D scores for the reconstructed volumetric images. By providing evidence under specific conditions, we demonstrate that the actual 3D score of the volumetric image can be obtained by combining these three pseudo-3D scores, allowing for comprehensive gradient updates on the entire 3D image. Furthermore, to ensure accuracy of the reconstructed 3D image, we incorporate 3D data consistency (e.g. SIRT-3D and K-space consistency) in the measurement space and effectively constrain the generation of our TOSM. During the reconstruction process, the powerful generative capability of the score-based model and the precise constraint of 3D data consistency complement each other, leading to

remarkable results to solve the 3D ill-posed inverse problems. Our approach offers four noteworthy contributions, which can be summarized as follows:

- We begin with an insightful observation. By utilizing a single pre-trained 2D score-based model, it allows us to calculate the weighting scores from three orthogonal directions to approximately estimate the 3D score. Remarkably, this approximation can be effectively determined through the combination of these three orthogonal directions.
- We present a groundbreaking approach to model the distribution of 3D volumetric images. By utilizing a single pre-trained 2D score-based model, we achieve a more accurate prediction of the 3D data distribution. To further enhance the efficiency and accuracy, we introduce a strategy to accelerate the computation of 3D scores, resulting in significantly reduced computational cost for the reconstruction process.
- We offer comprehensive theoretical derivations for the TOSM. They validate the rationale and effectiveness to train a 2D score function for 3D volumetric images. For the CT reconstruction task, we incorporate the Simultaneous Iterative Reconstruction Technique (SIRT) as a data consistency term to enhance the reconstruction capability. The exceptional convergence of TOSM ensures stable and deterministic reconstruction results.
- Our method is successfully applied to reconstruct medical images. It effectively addresses the challenging ill-posed inverse problems such as sparse-view CT and fast MRI reconstruction. The achieved results are truly remarkable, demonstrating the potential and effectiveness of our approach in advancing medical imaging.

II. RELATED WORK

A. Medical Ill-posed Inverse Problems

The fundamental challenge in medical image reconstruction lies in solving the ill-posed inverse problems. The imaging problem can be formulated as $\mathcal{P} = \mathcal{M}(v)$, where v represents the imaging object, \mathcal{M} models the measurement process, and \mathcal{P} is the measured data generated from v . In the context of CT imaging, \mathcal{P} represents the sinogram, while in MRI, \mathcal{P} represents the k-space data. The inverse problem involves finding \mathcal{M}^{-1} such that $v = \mathcal{M}^{-1}(\mathcal{P})$. However, this inverse problem is often ill-posed due to under-sampling during the data acquisition process. Therefore, it is crucial to develop effective methods to address such ill-posed inverse problems.

1) *Sparse-view CT Reconstruction*: Classical sparse-view CT reconstruction methods can be divided into two categories. The first category consists of the traditional methods that employ regularization techniques to promote the sparsity of the reconstructed images. For example, compressed sensing (CS) algorithms leverage the assumption that natural images are sparse in specific domains such as wavelet or total variation [19]. These methods assume that the underlying image can be well-represented using only a few coefficients in a suitable transform domain. The second category includes deep learning-based methods, which have emerged as a powerful

alternative. Approaches based on Convolutional Neural Networks (CNNs) (e.g., FBPCNet [20], Transformer-based MIST [9], and score-based methods [21]) have shown promising results in sparse-view CT reconstruction.

2) Fast MRI Reconstruction: Fast MRI reconstruction has gained significant attention in recent years, and various approaches have been proposed to accelerate the imaging process and improve reconstructed quality. One commonly explored direction is to leverage sparsity in MR images. CS-based approaches have been successfully applied to accelerate MRI by acquiring under-sampled k-space data and utilizing prior knowledge that MR images are sparse in certain domains [22]. These methods reconstruct high-quality images from significantly reduced data measurements. Additionally, deep learning-based methods have shown promising results. CNNs [23] and Generative Adversarial Networks (GANs) [24] have been trained to learn the mapping between under-sampled k-space data and fully-sampled images, enabling fast and accurate reconstruction. More recently, the score-based models have also demonstrated excellent results.

B. Denoising Score Matching Models

Score-based models are a class of probabilistic generative models that employ a forward diffusion process and a backward denoising process during training [21]. In the forward process, the noise of different scales is incrementally added to the input image, progressively degrading the image until it becomes pure Gaussian noise. In the backward generation process, the noise in the image is iteratively removed, effectively sampling the image from random Gaussian white noise. At each iteration, a neural network (e.g. U-Net) is employed to estimate the current noise. In the context of medical imaging, the inverse problem involves reconstructing the probability density distribution $p(\mathbf{x})$ of the reconstructed image \mathbf{x} [10].

1) Noise Conditioned Score Networks (NCSNs): The score function of the data probability density $p(\mathbf{x})$ is defined as a logarithmic gradient of the data probability density, $\nabla_{\mathbf{x}} \log p(\mathbf{x})$. The Langevin annealing algorithm is utilized to move the initial random probability density $p(\mathbf{x}_0)$ towards regions of high probability density [25]. The gradient of the logarithmic density serves as a force to guide the probability density into high-density regions. The iterative update equation is as follows:

$$\mathbf{x}_i = \mathbf{x}_{i-1} + \frac{\rho}{2} \nabla_{\mathbf{x}_{i-1}} \log p(\mathbf{x}_{i-1}) + \sqrt{\rho} \cdot \omega_i, \quad (1)$$

where $i \in (1, \dots, N)$, ρ controls the magnitude of the update in the direction of the score, \mathbf{x}_0 is sampled from a prior distribution, and $\omega_i \sim \mathcal{N}(0, \mathbf{I})$ represents random disturbance. Consequently, the scoring model $s_{\theta}(\mathbf{x}) \approx \nabla_{\mathbf{x}} \log p(\mathbf{x})$ can be trained to predict the derivatives of the probability density gradient, and the training loss function is defined as:

$$\mathcal{L}_{\text{sm}} = \mathbb{E}_{\mathbf{x} \sim p(\mathbf{x})} \|s_{\theta}(\mathbf{x}) - \nabla_{\mathbf{x}} \log p(\mathbf{x})\|_2^2. \quad (2)$$

2) Stochastic Differential Equations (SDEs): In the Stochastic Differential Equation Score Models (SDEs), the diffusion and restoration processes are treated as continuous operations, which are solved by using stochastic differential equations. The forward diffusion process of SDEs is defined as:

$$\partial \mathbf{x} = [\mathcal{F}(\mathbf{x}, t) - \sigma(t)^2 \cdot \nabla_{\mathbf{x}} \log p_t(\mathbf{x})] \cdot \partial t + \sigma(t) \cdot \Delta \hat{\omega}, \quad (3)$$

where \mathcal{F} is a function of \mathbf{x} and t to compute the drift coefficients, σ is a time-dependent function that computes diffusion coefficients, $\hat{\omega}$ represents the Brownian motion, and $\sigma(t)^2 \cdot \nabla_{\mathbf{x}} \log p_t(\mathbf{x})$ acts as the force to drive the probability density for high-density regions. Similarly to NCSNs, a neural network $s_{\theta}(\mathbf{x}, t) \approx \nabla_{\mathbf{x}} \log p_t(\mathbf{x})$ can be trained to estimate scores, and the loss function is defined as:

$$\mathcal{L}_{\text{sm}} = \mathbb{E}_{\mathbf{x} \sim p(\mathbf{x})} \|s_{\theta}(\mathbf{x}, t) - \nabla_{\mathbf{x}} \log p_t(\mathbf{x} | \mathbf{x}_0)\|_2^2. \quad (4)$$

In practice, small steps are used instead of continuous quantities, and an iterative solution is as follows:

$$\mathbf{x}_{t-1} = \mathbf{x}_t + [\mathcal{F}(\mathbf{x}, t) - \sigma(t)^2 \cdot \nabla_{\mathbf{x}} \log p_t(\mathbf{x})] \cdot \Delta t + \sigma(t) \cdot \Delta \hat{\omega}. \quad (5)$$

3) 3D Score-based Model: The 3D score-based model expands the scoring network from a 2D U-Net to a 3D U-Net architecture, enabling the score calculation in 3D space. However, due to the large number of voxels in a 3D volumetric image, handling computational cost becomes challenging, especially when the data dimension exceeds 64^3 [26]. Besides, Chung *et al.* mentions that it is difficult to apply 3D diffusion models to address medical imaging issues [6]. As a result, the current applications of 3D score-based models primarily concentrate on tasks such as point cloud denoising, small voxel generation, and structural prediction [27], rather than high-resolution voxel-based 3D reconstruction [28].

III. METHODOLOGY

A. TOSM Motivation

For a 3D volumetric image from one patient, we have intriguing observations. As shown in Fig. 2, the left panel showcases a 3D volumetric image and the corresponding histogram distribution. In the middle panel, we present transaxial, sagittal, and coronal views of the 3D image with enlarged regions of interest (ROIs). The ROIs in different views exhibit strikingly similar fine structural details, indicating a high level of similarity among slices from different planes (see the right panel). This shared structural coherence across different views underscores the consistency and integrity of the 3D volumetric data. Additionally, when examining the histogram distributions of image slices from three different planes, we find significant similarities. Furthermore, the histogram distributions of slices in the three planes closely resemble the histogram distribution of the entire 3D volumetric image. This consistency in histogram distributions reinforces the notion of shared features and overall coherence among slices in the volumetric image.

In light of the aforementioned observations, we can make the following hypothesis. Due to the striking similarity in feature structures and distributions of slices across different directions, the distributions of slices within the 3D volume can be approximated as equivalent from the point of view of big data. Consequently, a single neural network trained on 2D slices can be employed to model 3D data distribution, which is good to effectively leverage the shared information across different planes. These findings represent a significant advancement in 3D reconstruction, as they highlight the inherent coherence and consistency of the data in different plane views. By exploiting similarities in terms of structures and contents, we can streamline the reconstruction process

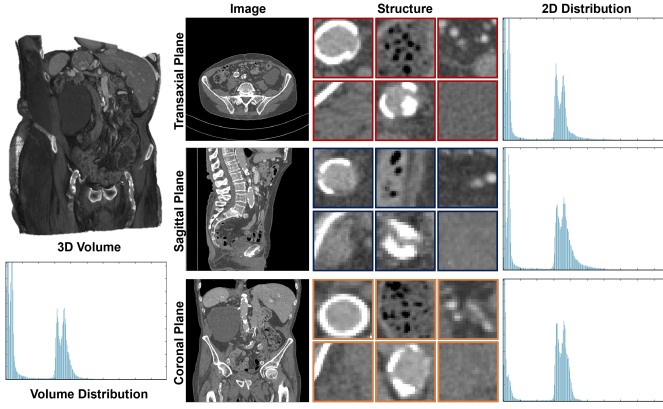


Fig. 2. Similarity among the histogram distribution of 3D volumetric images and the corresponding 2D distributions of slice images along three directions.

and achieve more efficient and robust results, enhancing the progress in medical imaging and other fields that rely on 3D volumetric reconstruction techniques.

B. TOSM Overview

The successful application of score-based models for 3D reconstruction poses a significant challenge to accurately recover the data distribution of 3D volumetric images while accounting for noise. Inspired by the observed similarity property of 3D volumetric images, we present a pioneering solution - the 2.5-order score-based model (TOSM). As shown in Fig. 3, our TOSM method builds upon conventional score-based models by training the scoring function to learn 2D distributions from 2D slices during the training phase. However, it is essential to highlight that relying solely on scores obtained from the coronal plane slice-by-slice, as typically done in the 2D score-based model during the reconstruction process (see Fig. 4), is an approximation. To overcome this limitation, our TOSM introduces a novel approach for computing 3D scores. During the reconstruction process, our TOSM leverages the trained scoring network to score each layer of the 3D volumetric image along the sagittal, coronal, and transaxial planes. This results in three 3D scores, precisely aligned with the dimensions of the reconstructed volumetric image.

However, a challenge emerges as these 3D scores alone cannot entirely represent the actual scores independently due to the lack of inter-slice information. To address this issue, TOSM adopts a weighted sum of these 3D scores, meticulously considering the spatial relationships and dependencies between adjacent slices. This approach enables us to obtain an authentic 3D score for the reconstructed volumetric image, as the weighting strategy incorporates 3D scores while taking into account the inter-slice connections from three different planes. In essence, the proposed TOSM approach adeptly tackles the limitations of conventional score-based models, significantly enhancing the accuracy of 3D reconstruction by effectively incorporating vital inter-slice information and comprehensively considering the spatial context of the volumetric images.

C. TOSM Theory

The primary challenge in utilizing the score-based models for 3D reconstruction is how to accurately model the data distribution of 3D volumetric images from noise. In this paper, we present an approach called 2.5-order score-based model (TOSM) to address this challenge. To begin, we consider three mutually orthogonal directions in 3D space: $x \in \mathbb{R}$, $y \in \mathbb{R}$, and $z \in \mathbb{R}$. We define the 3D volumetric image as $\mathbf{v}(x, y, z) \in \mathbb{R}$, where $\mathbf{v}(x, y, z)$ represents an element of the 3D volumetric image at (x, y, z) . In the following, we omit the position dependency and denote the element as \mathbf{v} when it does not cause confusion. Our first task is to model the probability density, $p(\mathbf{v})$, of the 3D volumetric images. For this purpose, we define $g_x(y, z) \in \mathbb{R}^2$, $h_y(x, z) \in \mathbb{R}^2$, and $f_x(x, y) \in \mathbb{R}^2$ as the 2D distributions of the $y-z$, $x-z$, and $x-y$ planes, respectively. The Dirac function $\delta(\cdot)$ plays a crucial role in the modeling process, and we define the data distribution of the volumetric images from three different directions as follows:

$$p(\mathbf{v}) = \int_{-\infty}^{+\infty} \delta(x-w) g_{x=w}(y, z) dw, \quad (6)$$

$$p(\mathbf{v}) = \int_{-\infty}^{+\infty} \delta(y-w) h_{y=w}(x, z) dw, \quad (7)$$

$$p(\mathbf{v}) = \int_{-\infty}^{+\infty} \delta(z-w) f_{z=w}(x, y) dw. \quad (8)$$

Combining these three approaches, we express the distribution $p(\mathbf{v})$ as follows:

$$[p(\mathbf{v})]^{\alpha+\beta+\gamma} = \left[\int_{-\infty}^{+\infty} \delta(x-w) g_{x=w}(y, z) dw \right]^{\alpha} \times \left[\int_{-\infty}^{+\infty} \delta(y-w) h_{y=w}(x, z) dw \right]^{\beta} \times \left[\int_{-\infty}^{+\infty} \delta(z-w) f_{z=w}(x, y) dw \right]^{\gamma}. \quad (9)$$

Due to the similarity observed in the 2D slice distributions in different planes of the same volume, we can approximate the distributions in different planes using the same function. Therefore, we make the following approximation:

$$[p(\mathbf{v})]^{\alpha+\beta+\gamma} = \left[\int_{-\infty}^{+\infty} \delta(x-w) f_{x=w}(y, z) dw \right]^{\alpha} \times \left[\int_{-\infty}^{+\infty} \delta(y-w) f_{y=w}(x, z) dw \right]^{\beta} \times \left[\int_{-\infty}^{+\infty} \delta(z-w) f_{z=w}(x, y) dw \right]^{\gamma}. \quad (10)$$

To obtain scores, which correspond to the gradients of the logarithmic data distribution, we simultaneously take the logarithm and gradient on both sides of (10) and set the hyperparameters such that $\alpha + \beta + \gamma = 1$:

$$\begin{aligned} \nabla_{\mathbf{v}} \log p(\mathbf{v}) = & \alpha \nabla_{y,z} \log \left[\int_{-\infty}^{+\infty} \delta(x-w) f_{x=w}(y, z) dw \right] \\ & + \beta \nabla_{x,z} \log \left[\int_{-\infty}^{+\infty} \delta(y-w) f_{y=w}(x, z) dw \right] \\ & + \gamma \nabla_{x,y} \log \left[\int_{-\infty}^{+\infty} \delta(z-w) f_{z=w}(x, y) dw \right]. \end{aligned} \quad (11)$$

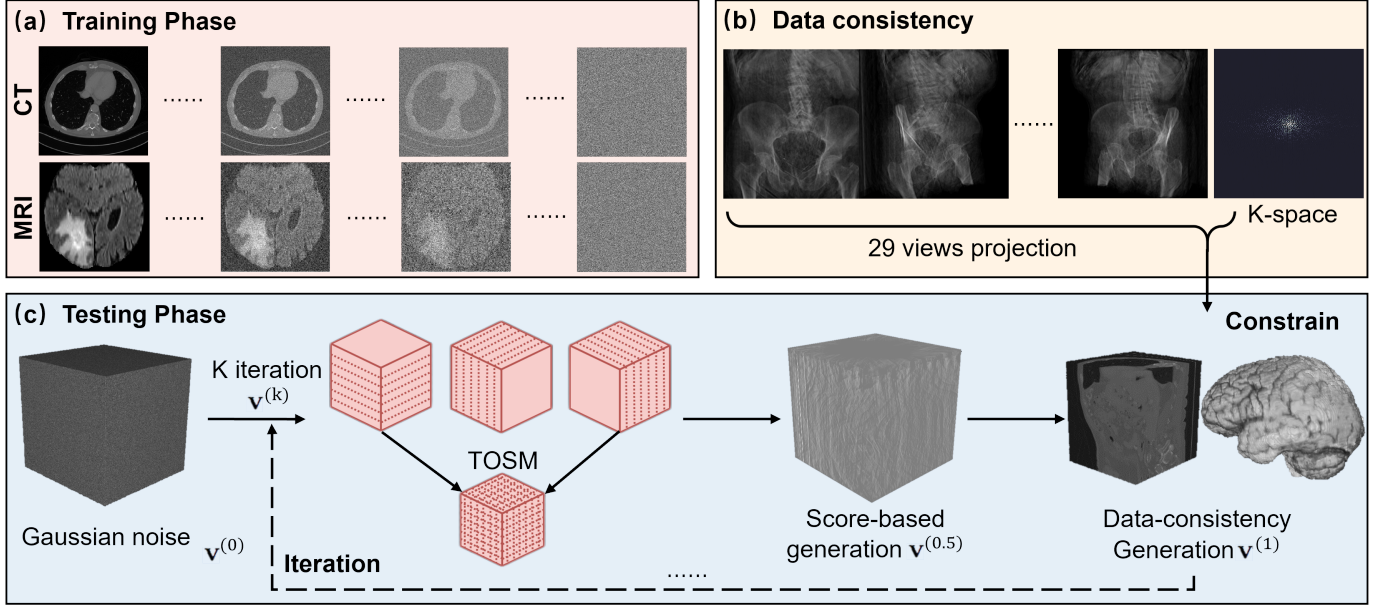


Fig. 3. The TOSM method is employed to solve the inverse problem through a well-defined pipeline. Initially, 3D Gaussian noise is iteratively generated using a 2.5-order score model. Subsequently, a data consistency constraint is introduced. By iteratively combining these two processes, high-quality 3D reconstruction is achieved.

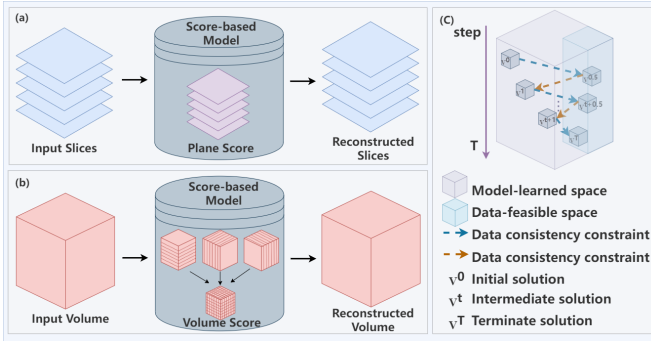


Fig. 4. Comparison of the traditional 2D score-based models and our TOSM for 3D Reconstruction. (a) Existing 2D score-based model for 3D reconstruction, where the 3D volumetric image is sliced into 2D slices and subsequently stacked together. (b) The process of 3D volumetric reconstruction using TOSM: the entire volume is inputted into the model. The pre-trained 2D score-based model calculates scores in three mutually orthogonal directions. (c) The optimization process of TOSM.

In practical applications, x , y , and z are discrete variables. Using the Kronecker delta function δ' , we can discretize (11) as follow:

$$\begin{aligned} \nabla_{\mathbf{v}} \log p(\mathbf{v}) = & \alpha \nabla_{y,z} \log \sum_{k=0}^K \left[\delta'_{xk} f_{x=k}(y, z) \right] \\ & + \beta \nabla_{x,z} \log \sum_{j=0}^J \left[\delta'_{yj} f_{y=j}(x, z) \right] \\ & + \gamma \nabla_{x,y} \log \sum_{q=0}^Q \left[\delta'_{zq} f_{z=q}(x, y) \right], \end{aligned} \quad (12)$$

where K , J , and Q represent the slice numbers of the $y-z$,

$x-z$, and $x-y$ planes, respectively. Since the 2D data distributions of each plane are subsets of the same 3D distribution in our proposed TOSM, 3D scores can be predicted using a single pre-trained 2D network, denoted as S_{θ} , where the network parameters θ remain the same. Consequently, we can reach the following equation (13), where \mathbf{v}_t represents an initial 3D random noise obeying a Gaussian normal distribution, and t is the total number of diffusion steps:

$$\begin{aligned} \nabla_{\mathbf{v}_t} \log p(\mathbf{v}_t) \approx & \alpha \sum_{k=0}^K S_{\theta}(\mathbf{v}_t[k, :, :], t) + \beta \sum_{j=0}^J S_{\theta}(\mathbf{v}_t[:, j, :], t) \\ & + \gamma \sum_{q=0}^Q S_{\theta}(\mathbf{v}_t[:, :, q], t). \end{aligned} \quad (13)$$

By employing the above transformations, the 3D score problem is converted into the computation of 2D scores in three directions. As a result, our proposed TOSM can leverage a trained 2D score-based model to compute the overall 3D scores.

D. TOSM Applications

As illustrated in Fig. 3, TOSM can effectively address ill-posed inverse problems in medical imaging. The key to solve an ill-posed inverse problem is to find the solution of $\mathbf{v} = \mathcal{M}^{-1}(\mathcal{P})$, where \mathcal{M} is an operator to generate the measured data \mathcal{P} , and \mathbf{v} is the scanned object. Due to the ill-posed nature of this problem, we adopt a regularized iterative approach:

$$\mathbf{v}^* = \underset{\mathbf{v}}{\operatorname{argmin}} \frac{1}{2} \|\mathcal{P} - \mathcal{M}\mathbf{v}\|_2^2 + \frac{\eta}{2} R(\mathbf{v}), \quad (14)$$

where $R(\cdot)$ is a suitable regularization, and η is the regularization factor to balance the data fidelity and regularization prior.

Here, we use a score from the 2.5-order score-based model as the regularization term to guide the optimizing process,

$$\mathbf{v}^* = \underset{\mathbf{v}}{\operatorname{argmin}} \frac{1}{2} \|\mathcal{P} - \mathcal{M}\mathbf{v}\|_2^2 + \frac{\eta}{2} \nabla_{\mathbf{v}} \log p(\mathbf{v}). \quad (15)$$

As illustrated in Fig. 4, the volumetric image generated by the score-based model resides in the space learned by the model, and it consists of the feasible data space. Actually, the solution \mathbf{v}^{d+1} can be iteratively updated in two steps:

$$\mathbf{v}^{d+0.5} = \underset{\mathbf{v}}{\operatorname{argmin}} \frac{1}{2} \|\mathcal{P} - \mathcal{M}\mathbf{v}\|_2^2 + \frac{\psi}{2} \|\mathbf{v} - \mathbf{v}^d\|_2^2, \quad (16)$$

$$\mathbf{v}^{d+1} = \underset{\mathbf{v}}{\operatorname{argmin}} \frac{1}{2} \|\mathbf{v} - \mathbf{v}^{d+0.5}\|_2^2 + \frac{\eta}{2} \nabla_{\mathbf{v}} \log p(\mathbf{v}), \quad (17)$$

where the symbol ψ serves as a factor and d represents the current iteration number. To tackle (16) in sparse-view CT and fast MRI reconstruction tasks, we employ different iteration strategies as data consistency measures to constrain the reconstruction process. Specifically, for sparse-view CT reconstruction, we utilize the classical SIRT method to solve (16). Conversely, in MRI reconstruction tasks, we adopt the k-space consistency to enforce constraints on the reconstruction process. Equation (17) represents a score model-based regularization prior that can be updated using the trained 3D scores. Through iterative updates of the reconstructed volumetric image, we enhance the consistency between the generated volumetric image and the observed data measurements. By incorporating these data consistency measures, the TOSM framework can resolve the ill-posed inverse problems in medical imaging, leading to improved reconstruction accuracy and robustness.

1) Sparse-view CT Reconstruction: In the sparse-view CT reconstruction task, the available measured views in the projection domain are sparse and incomplete, resulting in sparse-view artifacts. Inspired by the iterative reconstruction method SIRT [29], we want to generate a current volumetric image that aligns with the original projections from each view. To achieve this goal, we define initial parameters for data consistency. Specifically, p_a represents a projection value for a^{th} x-ray path, \mathbf{v}_n denotes the n^{th} pixel of \mathbf{v} , and N represents the number of pixels within \mathbf{v} . m_{an} represents a weight factor, indicating the contribution of \mathbf{v}_n for a^{th} ray. We begin by calculating the estimated projection value for the x-ray path a :

$$p_a^* = \sum_{n=1}^N m_{an} \mathbf{v}_n^{(d)}, \quad (18)$$

where b represents the set of x-ray paths across all projection views. Subsequently, we modify the value of the b part using the following equation:

$$C_b = \sum_{a \in b} \frac{p_a - \sum_{n=1}^N m_{an} \mathbf{v}_n^{(d)}}{\sum_{n=1}^N m_{an}} m_{ab}. \quad (19)$$

Finally, the SIRT is used to update by the following expression:

$$\mathbf{v}_n^{(d+1)} = \mathbf{v}_n^{(d)} + \frac{C_b}{\sum_{a \in b} m_{an}}, \quad (20)$$

and it can be further written as

$$\mathbf{v}_n^{(d+1)} = \mathbf{v}_n^{(d)} + \frac{\sum_{a \in b} \frac{p_a - \sum_{n=1}^N m_{an} \mathbf{v}_n^{(d)}}{\sum_{n=1}^N m_{an}} m_{an}}{\sum_{a \in b} m_{an}}. \quad (21)$$

2) Fast MRI Reconstruction: In fast MRI reconstruction, we simplify the calculation by dividing the data consistency into two parts: one in the image domain and the other in K-space. The data consistency is defined as follows:

$$\mathbf{v}^{(d+1)} = (I - \gamma_1 M_2^* M_2) \mathbf{v}^{(d)} + M_2^* \mathcal{P}^*, \quad (22)$$

where $\gamma_1 \in [0, 1]$, M_2^* is the Hermitian conjugate of M_2 , M_2 and M_2^* represent the 2D discrete Fourier forward and inverse transformations, and \mathcal{P}^* represents the measured data in k-space. Inspired by the work of Chung *et. al.* [12], the data consistency constraints need to satisfy a non-extended mapping property. The details on the pertaining to Eq. (22) can refer to [30].

In MRI reconstruction, since the data are complex values, we need to consider the phase information. Unlike CT reconstruction, MRI data cannot be directly processed using neural networks [31]. To address this, we divide the data into real and imaginary parts, treating them in different channels. This approach effectively improves the stability of the reconstruction process [12].

IV. EXPERIMENTAL SETUP AND RESULTS

In this section, we present the experimental validation and show our study results. We begin by introducing the involved datasets. Then, we provide a comprehensive description of the key parameters and the experimental setup. Finally, we perform a comparative evaluation of our method against the state-of-the-art approaches, focusing on addressing the challenges of sparse-view CT and fast MRI reconstruction.

A. Datasets and Implementation Details

1) Datasets: We utilize the Mayo Clinic abdomen images from the AAPM Low Dose CT Grand Challenge by McCollough *et. al.* [32] for sparse-view CT reconstruction. The dataset comprises normal-dose CT scans from 10 patients, with 9 patients for training and one patient for evaluation. The training dataset consists of 4608 slices, and each of them has 1.0 mm thick, covering a pixel grid of 512×512 . For the sparse-view testing set, we use cone-beam scanning geometry, where the distances from the rotation center to the source and detector are set as 50cm and 50cm, respectively. A flat panel detector is assumed with 1024×1024 pixels, and each pixel covers an area of 0.08×0.08 mm². We generate only 29 views evenly distributed over 360 degrees for testing in this study.

In the MRI experiment, we utilize the publicly available fast MRI reconstruction dataset from the multi-modal brain tumor image segmentation benchmark (BRATS) 2018 [33]. We employ the pre-trained score function on fast MRI knee datasets [34]. Thus, it does not need to process the MRI training data. Our training process follows the methodology outlined in [11]. In the testing phase, we select brain images from a single patient with dimensions of $155 \times 240 \times 240$. By the zero-padding, we obtain $240 \times 240 \times 240$ brain images.

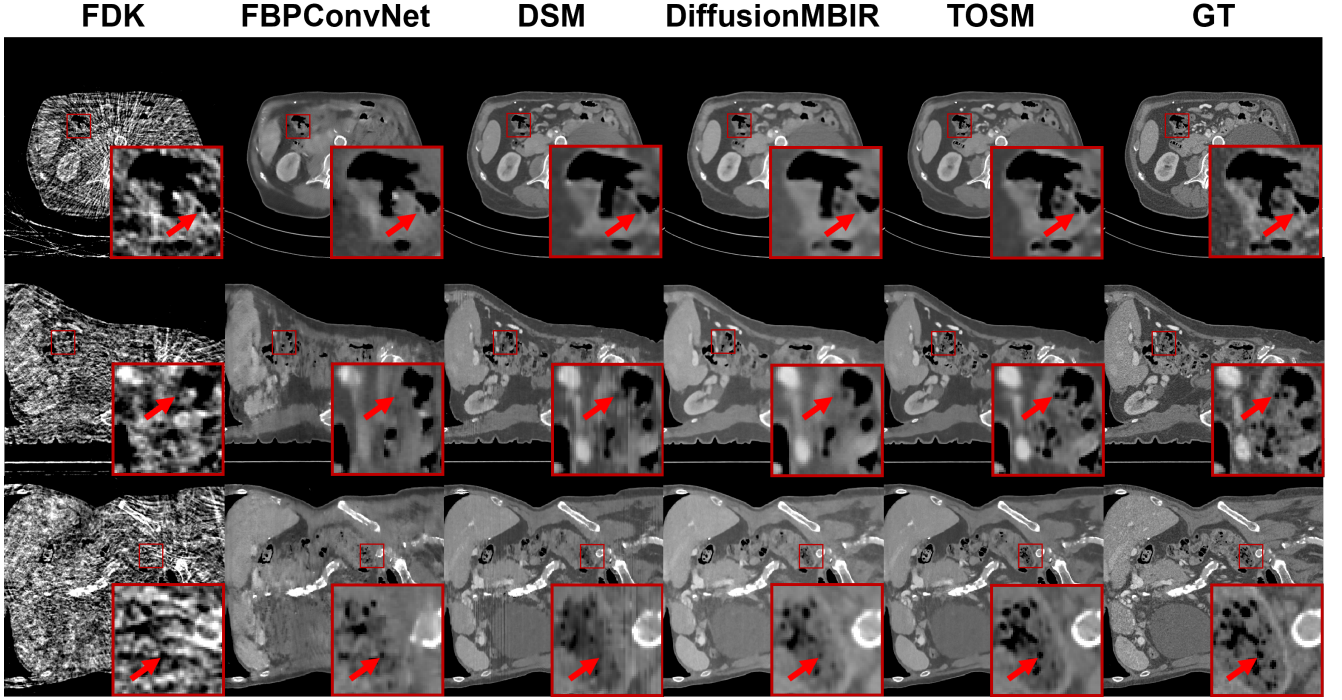


Fig. 5. Representative reconstructed results of cone-beam CT from 29 views by different methods. From top to bottom, the rows correspond to the transaxial, sagittal, and coronal planes. The first to fifth columns correspond to different reconstruction methods, and the last column shows the ground truth (GT) images.

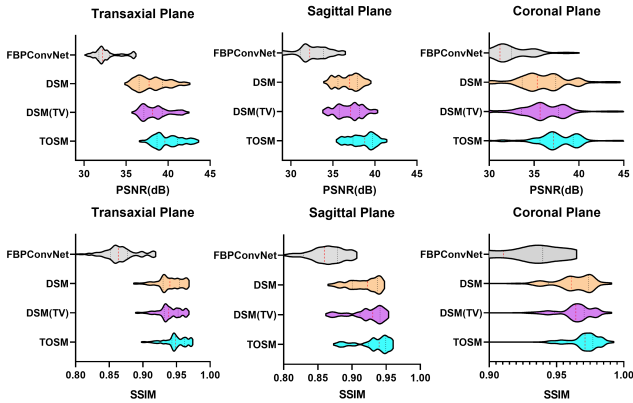


Fig. 6. The violin plot for the statistical results of different methods, including FBPCConvNet, DSM, DiffusionMBIR, and our TOSM. It is obvious that our TOSM achieves the best results.

2) Model Training and Parameter Selection: For model training, we employ the Adam algorithm with a learning rate of 10^{-3} . Our method is implemented in Python, utilizing the ASTRA toolbox [35] and PyTorch. The traditional score-based models for 3D volumetric reconstruction often require a high computational cost. However, our method exhibits a capability to handle reconstruction tasks of size $512 \times 512 \times 512$ on a single RTX 3090 GPU. Hence, all experiments in this study are conducted using an RTX 3090 for computation.

To introduce a diverse range of noise levels, we generate twelve different noise levels. During the training phase, random noise corresponding to these twelve levels is added to each image and then fed into the network. The training process

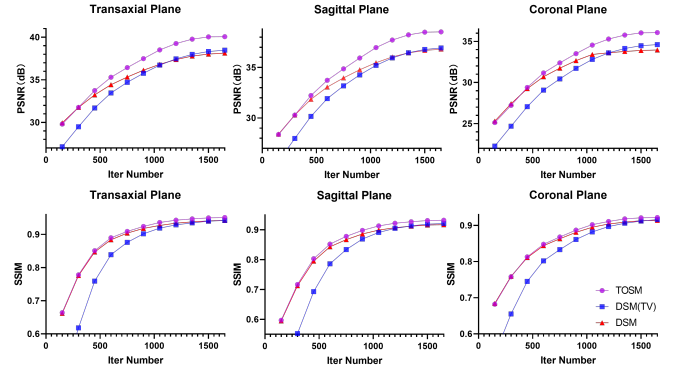


Fig. 7. The convergence plots of PSNR and SSIM with respect to the number of iterations in the testing phase.

iterates 100,000 times to ensure robust learning. During the reconstruction phase, we generate volumetric images at each of the twelve noise levels, 150 iterations are employed for each level. In each iteration, we enforce data consistency using the SIRT algorithm with 20 iterations. To reach a balance between the generative capability of the score model and the constraint of data consistency, we assign weights of 0.5 to both of the factors.

To quantitatively evaluate algorithm performance, two standard evaluation metrics are computed: peak signal-to-noise ratio (PSNR) and structural similarity (SSIM). We also generate visual representations of the reconstructed 3D volumetric images to compare their spatial and structural characteristics. Our goal is to demonstrate the effectiveness and superiority of

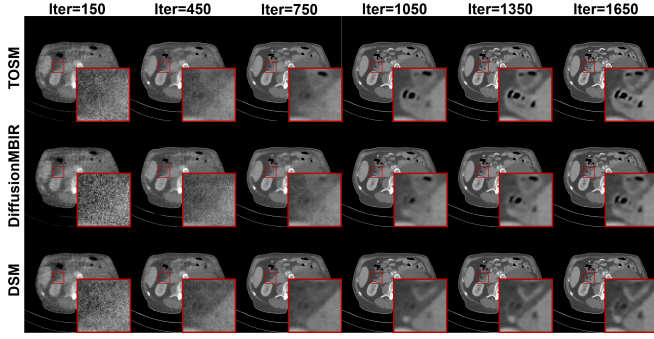


Fig. 8. Reconstructed images of three scoring models with respect to different iteration numbers. Clearly, TOSM outperforms the other scoring model methods at any iteration number.

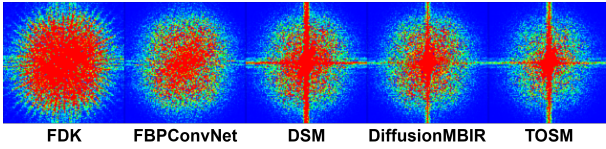


Fig. 9. The noise power spectra (NPS) plots of different methods. The central region of the plots represents low-frequency noise components, while the outer region represents high-frequency noise components.

our approach in addressing challenges related to sparse-view CT and fast MRI reconstruction. We rigorously follow this experimental setup to comprehensively evaluate and compare our method against existing techniques.

B. Sparse-view CT Reconstruction

In this experiment, the comparison methods include the traditional Feldkamp-Davis-Kress (FDK) [35], CNN-based FBPCConvNet [20], denoising score-based model (DSM) [25] and DiffusionMBIR [18]. Particularly, the DiffusionMBIR is constrained with the DSM and total variation (TV). Figure 5 shows the reconstructed results from 29 projection views with different methods.

The FDK algorithm, as one of the classical analytic reconstruction methods, reconstructs low-quality images in the transaxial, sagittal, and coronal planes with obvious streaky sparse-view artifacts. Meanwhile, the FBPCConvNet, trained solely on transaxial slices, only recovers rough image contours, resulting in the loss of fine details. The stacked sagittal and coronal images suffer from even more severe information loss with slice inconsistency. The DSM is one of the classical score-based reconstruction methods, by combining prior data distribution regularization and data consistency, it shows promising results in the transaxial plane but still has distortions in the details. In the stacked sagittal and coronal slices, significant inaccuracies lead to distortions and errors in the magnified ROIs. The DiffusionMBIR approach is designed to address the inter-slice inconsistency in 3D reconstruction using a score-based model. It incorporates TV in the z-direction to constrain the generation of sagittal and coronal planes. However, this approach does not explicitly model the 3D volumetric images, and the generated results are not as effective as our TOSM method. In contrast, our

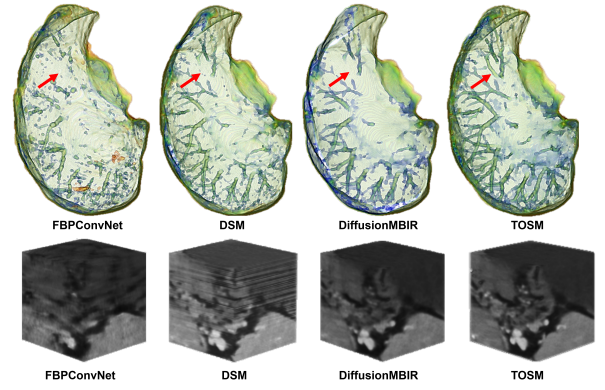


Fig. 10. Visualization of representative 3D volumetric reconstruction results. The top row are 3D volumetric renderings of the lung CT from different methods, where the tubular structures represent pulmonary blood vessels and the red arrows indicate notable features. The bottom row are 3D ROI rendering of $100 \times 100 \times 100$ volumetric images.

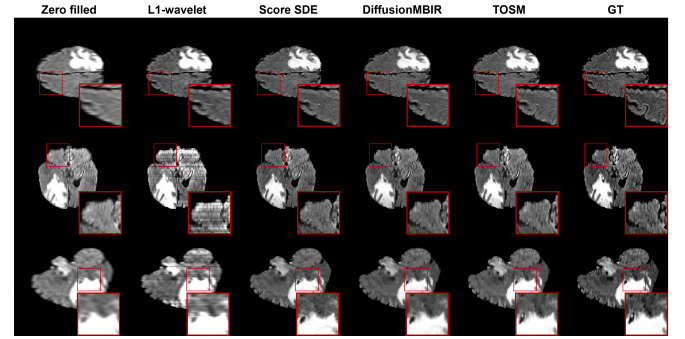


Fig. 11. Representative results of fast MRI reconstruction from $\times 15$ acceleration Gaussian 1D sub-sampled data. The first row is the primary plane, and the second row and third rows are auxiliary planes. The first to fifth columns correspond to different reconstruction methods, and the last column shows the GT images

TOSM demonstrates outstanding results in 3D volumetric reconstruction. In the transaxial slice, the incorporation of complementary information from the sagittal and coronal views significantly improves image quality. The sparse-view artifacts are minimized in the reconstructed images, and the details are accurately restored. In the sagittal and coronal planes, our method stands out as the only one capable of producing accurate reconstructions. The details in the ROIs precisely match the ground truths, demonstrating exceptional performance to solve the inter-slice inconsistency issue and highlighting the effectiveness of our approach.

Additionally, quantitative analysis is performed and the results are in Fig. 6 and Table II. Our TOSM method outperforms the FDK, FBPCConvNet, DSM, and DiffusionMBIR in 3D volumetric reconstruction. Particularly, our TOSM achieves significant improvements in the sagittal and coronal planes compared to the transaxial plane. This observation verifies the superior 3D reconstruction capabilities of our approach over other methods.

Moreover, Figs. 7 and 8 demonstrate that the TOSM has fast convergence compared to the DSM and DiffusionMBIR. Obviously, the purple line representing TOSM is consistently above those of the DSM and DiffusionMBIR. With the same

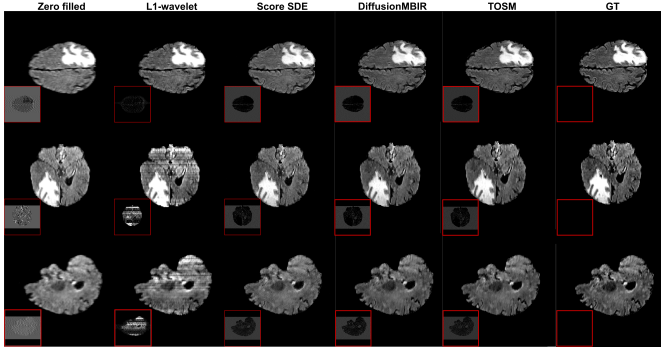


Fig. 12. Similar to Fig. 11 but from $\times 2$ acceleration Gaussian 1D sub-sampled data.

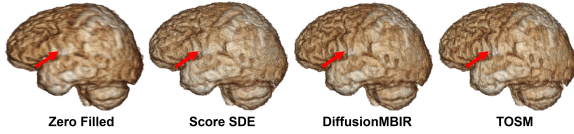


Fig. 13. 3D volumetric rendering of the brain MRI. The red arrows are used to highlight remarkable channel features within the brain.

number of iterations, TOSM has a better performance. Besides, Fig. 9 compares the noise power spectrum (NPS) [36]. It is seen that the DSM, DiffusionMBIR, and our TOSM significantly improve NPS compared to the other methods, evidenced by the star-shaped pattern observed in the plots. Especially, our TOSM yields the best superior results, outperforming the others by a considerable margin.

Furthermore, to visually showcase the efficacy of our method in 3D reconstruction tasks, we present representative visualization results in Fig. 10. It shows the connectivity of pulmonary vessels and smooth continuity of 3D structures, with noteworthy features indicated by red arrows. Clearly, our TOSM results demonstrate substantially stronger vascular connectivity when compared to other methods, underscoring its exceptional ability to capture intricate details of pulmonary blood vessels. These results unequivocally establish the TOSM as the top approach for 3D volumetric reconstruction among the compared methods.

TABLE I
QUANTITATIVE EVALUATION RESULTS FOR SPARSE-VIEW CT RECONSTRUCTION

Method	PSNR(dB) and SSIM		
	Transaxial*	Sagittal	Coronal+
FDK	21.33 / 0.367	29.71 / 0.264	16.91 / 0.269
FBPConvNet	32.76 / 0.872	31.55 / 0.844	29.08 / 0.844
DSM	38.14 / 0.938	36.82 / 0.917	33.96 / 0.914
DiffusionMBIR	38.52 / 0.943	36.89 / 0.926	34.56 / 0.916
TOSM	40.06 / 0.954	38.52 / 0.933	36.06 / 0.922

C. Fast MRI Reconstruction

To comprehensively evaluate the effectiveness of our method in undersampled MRI reconstruction, experiments are conducted on 1D uniformly and Gaussian 1D random sub-sampling scenarios. Specifically, we retain only 15% of the

TABLE II
QUANTITATIVE EVALUATION RESULTS FOR FAST MRI RECONSTRUCTION

Method	PSNR(dB) and SSIM		
	Transaxial*	Sagittal	Coronal+
FASTMRI X15 GAUSSIAN 1D RECONSTRUCTION			
Zero-filled	27.79 / 0.712	25.87 / 0.551	27.78 / 0.711
L1-wavelet	29.88 / 0.664	27.85 / 0.617	29.73 / 0.661
Score SDE	31.54 / 0.815	29.54 / 0.708	31.41 / 0.812
DiffusionMBIR	32.27 / 0.829	30.11 / 0.730	32.01 / 0.827
Our	32.72 / 0.846	30.67 / 0.760	32.55 / 0.844
FASTMRI X2 UNIFORM 1D RECONSTRUCTION			
Zero-filled	29.95 / 0.787	27.98 / 0.679	29.90 / 0.788
L1-wavelet	30.57 / 0.757	29.31 / 0.707	30.49 / 0.751
Score SDE	34.78 / 0.893	32.86 / 0.830	34.76 / 0.892
DiffusionMBIR	34.99 / 0.901	33.12 / 0.838	34.98 / 0.896
Our	35.95 / 0.915	33.93 / 0.864	35.83 / 0.913

auto-calibration signal (ACS) region at the center and sample only half of the k-space lines, resulting in acceleration factors of approximately $\times 2$ and $\times 15$, respectively.

The results of the $\times 15$ accelerated reconstruction, as depicted in Fig. 11, demonstrate remarkable similarities to high-quality CT scans. Particularly, the transaxial plane showcases the most favorable reconstruction performance. In comparison to the L1-wavelet algorithm [37], which introduces severe discontinuities and artifacts in the other two planes, our approach exhibits superior performance compared to 2D score-based models. Notably, our method achieves more accurate details in the coronal and sagittal planes when compared to the current baseline method DiffusionMBIR. The quantitative statistical results in Table II further confirm the superior reconstruction quality of our proposed TOSM method in comparison to other model-based methods.

Additionally, the results of $\times 2$ acceleration (see Fig. 12) exhibit high-fidelity reconstructions on all three anatomical planes. Conversely, the L1-wavelet method encounters severe discontinuities and artifacts in the other two planes. Again, the quantitative statistical results in Table II support the conclusion that our TOSM method outperforms other comparison methods. Furthermore, we provide a 3D rendering of the MRI reconstruction result in Fig. 13, focusing on the region indicated by red arrows. Notably, the contours generated by our TOSM method exhibit greater clarity and accuracy, while the other methods have different degrees of distortions.

The experimental results offer compelling evidences for the effectiveness and generalizability of our approach in fast MRI reconstruction tasks. By effectively addressing the reconstruction challenges associated with downsampled k-space data, our TOSM method outperforms existing algorithms, resulting in high-quality reconstructions that faithfully preserve essential structural information in 3D volumetric images.

V. CONCLUSION

In this study, we introduce a 2.5-order score-based model (TOSM) as a promising and innovative solution to address 3D ill-posed inverse problems. The TOSM demonstrates its remarkable ability to accurately compute 3D scores by leveraging data distribution learned from 2D planes through a pre-trained scoring network. This unique approach enables

efficient global updates of the 3D volumetric images without imposing significant computational overhead.

The experimental results have consistently demonstrated the effectiveness and generalizability of our method across various tasks, including few-view CT reconstruction on the AAPM datasets and fast MRI reconstruction with $\times 2$ and $\times 15$ acceleration. Remarkably, our method has a strong capability to handle the challenge of inter-slice inconsistency, resulting in an outstanding performance to solve typical 3D inverse problems.

REFERENCES

- [1] H. Greenspan, B. Van Ginneken, and R. M. Summers, "Guest editorial deep learning in medical imaging: Overview and future promise of an exciting new technique," *IEEE Transactions on Medical Imaging*, vol. 35, no. 5, pp. 1153–1159, 2016.
- [2] H. Zhang, D. Zeng, H. Zhang, J. Wang, Z. Liang, and J. Ma, "Applications of nonlocal means algorithm in low-dose x-ray ct image processing and reconstruction: a review," *Medical Physics*, vol. 44, no. 3, pp. 1168–1185, 2017.
- [3] H. Chen, Y. Zhang, M. K. Kalra, F. Lin, Y. Chen, P. Liao, J. Zhou, and G. Wang, "Low-dose ct with a residual encoder-decoder convolutional neural network," *IEEE Transactions on Medical Imaging*, vol. 36, no. 12, pp. 2524–2535, 2017.
- [4] W. Wu, D. Hu, C. Niu, H. Yu, V. Vardhanabhuti, and G. Wang, "Drone: dual-domain residual-based optimization network for sparse-view CT reconstruction," *IEEE Transactions on Medical Imaging*, vol. 40, no. 11, pp. 3002–3014, 2021.
- [5] G. Yang, S. Yu, H. Dong, G. Slabaugh, P. L. Dragotti, X. Ye, F. Liu, S. Arridge, J. Keegan, Y. Guo, *et al.*, "Dagan: deep de-aliasing generative adversarial networks for fast compressed sensing MRI reconstruction," *IEEE Transactions on Medical Imaging*, vol. 37, no. 6, pp. 1310–1321, 2017.
- [6] H. Chung, D. Ryu, M. T. McCann, M. L. Klasky, and J. C. Ye, "Solving 3d inverse problems using pre-trained 2d diffusion models," in *Proceedings of the IEEE/CVF Conference on Computer Vision and Pattern Recognition*, pp. 22542–22551, 2023.
- [7] H. Gupta, K. H. Jin, H. Q. Nguyen, M. T. McCann, and M. Unser, "Cnn-based projected gradient descent for consistent ct image reconstruction," *IEEE Transactions on Medical Imaging*, vol. 37, no. 6, pp. 1440–1453, 2018.
- [8] X. Ying, H. Guo, K. Ma, J. Wu, Z. Weng, and Y. Zheng, "X2ctgan: reconstructing ct from biplanar x-rays with generative adversarial networks," in *Proceedings of the IEEE/CVF Conference on Computer Vision and Pattern Recognition*, pp. 10619–10628, 2019.
- [9] J. Pan, H. Zhang, W. Wu, Z. Gao, and W. Wu, "Multi-domain integrative swin transformer network for sparse-view tomographic reconstruction," *Patterns*, p. 100498, 2022.
- [10] Y. Song, L. Shen, L. Xing, and S. Ermon, "Solving inverse problems in medical imaging with score-based generative models," in *International Conference on Learning Representations*, 2022.
- [11] Y. Song, J. Sohl-Dickstein, D. P. Kingma, A. Kumar, S. Ermon, and B. Poole, "Score-based generative modeling through stochastic differential equations," in *International Conference on Learning Representations*, 2021.
- [12] H. Chung and J. C. Ye, "Score-based diffusion models for accelerated MRI," *Medical Image Analysis*, vol. 80, p. 102479, 2022.
- [13] X. Zheng, S. Ravishanker, Y. Long, and J. A. Fessler, "Pwls-ultra: An efficient clustering and learning-based approach for low-dose 3d ct image reconstruction," *IEEE Transactions on Medical Imaging*, vol. 37, no. 6, pp. 1498–1510, 2018.
- [14] C. J. F. Reyneke, M. Lüthi, V. Burdin, T. S. Douglas, T. Vetter, and T. E. Mutsaers, "Review of 2-d/3-d reconstruction using statistical shape and intensity models and x-ray image synthesis: Toward a unified framework," *IEEE Reviews in Biomedical Engineering*, vol. 12, pp. 269–286, 2018.
- [15] U. Khan, A. Yasin, M. Abid, I. Shafi, and S. A. Khan, "A methodological review of 3d reconstruction techniques in tomographic imaging," *Journal of Medical Systems*, vol. 42, no. 10, p. 190, 2018.
- [16] A. Angelopoulou, A. Psarrou, J. Garcia-Rodriguez, S. Orts-Escolano, J. Azorin-Lopez, and K. Revett, "3d reconstruction of medical images from slices automatically landmarked with growing neural models," *Neurocomputing*, vol. 150, pp. 16–25, 2015.
- [17] I. Selesnick, "Total variation denoising (an mm algorithm)," *NYU Polytechnic School of Engineering Lecture Notes*, vol. 32, 2012.
- [18] S. Lee, H. Chung, M. Park, J. Park, W.-S. Ryu, and J. C. Ye, "Improving 3d imaging with pre-trained perpendicular 2d diffusion models," *arXiv preprint arXiv:2303.08440*, 2023.
- [19] W. Wu, Y. Zhang, Q. Wang, F. Liu, P. Chen, and H. Yu, "Low-dose spectral ct reconstruction using image gradient 0-norm and tensor dictionary," *Applied Mathematical Modelling*, vol. 63, pp. 538–557, 2018.
- [20] K. H. Jin, M. T. McCann, E. Froustey, and M. Unser, "Deep convolutional neural network for inverse problems in imaging," *IEEE Transactions on Image Processing*, vol. 26, no. 9, pp. 4509–4522, 2017.
- [21] Y. Song and S. Ermon, "Improved techniques for training score-based generative models," *Advances in Neural Information Processing Systems*, vol. 33, pp. 12438–12448, 2020.
- [22] M. Lustig, D. L. Donoho, J. M. Santos, and J. M. Pauly, "Compressed sensing mri," *IEEE Signal Processing Magazine*, vol. 25, no. 2, pp. 72–82, 2008.
- [23] B. Murugesan, S. Ramanarayanan, S. Vijayarangan, K. Ram, N. R. Jagannathan, and M. Sivaprakasam, "A deep cascade of ensemble of dual domain networks with gradient-based t1 assistance and perceptual refinement for fast mri reconstruction," *Computerized Medical Imaging and Graphics*, vol. 91, p. 101942, 2021.
- [24] S. Chen, S. Sun, X. Huang, D. Shen, Q. Wang, and S. Liao, "Data-consistency in latent space and online update strategy to guide gan for fast mri reconstruction," in *Machine Learning for Medical Image Reconstruction: Third International Workshop, MLMIR 2020, Held in Conjunction with MICCAI 2020, Lima, Peru, October 8, 2020, Proceedings 3*, pp. 82–90, Springer, 2020.
- [25] Y. Song and S. Ermon, "Generative modeling by estimating gradients of the data distribution," in *Advances in Neural Information Processing Systems* (H. Wallach, H. Larochelle, A. Beygelzimer, F. d'Alché-Buc, E. Fox, and R. Garnett, eds.), vol. 32, Curran Associates, Inc., 2019.
- [26] Z. Liu, H. Tang, Y. Lin, and S. Han, "Point-voxel cnn for efficient 3d deep learning," *Advances in Neural Information Processing Systems*, vol. 32, 2019.
- [27] S. Luo and W. Hu, "Diffusion probabilistic models for 3d point cloud generation," in *Proceedings of the IEEE/CVF Conference on Computer Vision and Pattern Recognition*, pp. 2837–2845, 2021.
- [28] X. Zeng, A. Vahdat, F. Williams, Z. Gojcic, O. Litany, S. Fidler, and K. Kreis, "Lion: Latent point diffusion models for 3d shape generation," *arXiv preprint arXiv:2210.06978*, 2022.
- [29] J. Gregor and T. Benson, "Computational analysis and improvement of sirt," *IEEE Transactions on Medical Imaging*, vol. 27, no. 7, pp. 918–924, 2008.
- [30] Z. Tang, M. Deng, C. Xiao, and J. Yu, "Projection onto convex sets super-resolution image reconstruction based on wavelet bi-cubic interpolation," in *Proceedings of 2011 International Conference on Electronic & Mechanical Engineering and Information Technology*, vol. 1, pp. 351–354, IEEE, 2011.
- [31] C. M. Hyun, H. P. Kim, S. M. Lee, S. Lee, and J. K. Seo, "Deep learning for undersampled mri reconstruction," *Physics in Medicine & Biology*, vol. 63, no. 13, p. 135007, 2018.
- [32] C. McCollough, "Overview of the low dose ct grand challenge," *Medical physics*, vol. 43, no. 6Part35, pp. 3759–3760, 2016.
- [33] B. H. Menze, A. Jakab, S. Bauer, J. Kalpathy-Cramer, K. Farahani, J. Kirby, Y. Burren, N. Porz, J. Slotboom, R. Wiest, *et al.*, "The multimodal brain tumor image segmentation benchmark (brats)," *IEEE Transactions on Medical Imaging*, vol. 34, no. 10, pp. 1993–2024, 2014.
- [34] J. Zbontar, F. Knoll, A. Sriram, T. Murrell, Z. Huang, M. J. Muckley, A. Defazio, R. Stern, P. Johnson, M. Bruno, *et al.*, "fastmri: An open dataset and benchmarks for accelerated mri," *arXiv preprint arXiv:1811.08839*, 2018.
- [35] W. Van Aarle, W. J. Palenstijn, J. De Beenhouwer, T. Altantzis, S. Bals, K. J. Batenburg, and J. Sijbers, "The astra toolbox: A platform for advanced algorithm development in electron tomography," *Ultramicroscopy*, vol. 157, pp. 35–47, 2015.
- [36] M. F. Kijewski and P. F. Judy, "The noise power spectrum of ct images," *Physics in Medicine & Biology*, vol. 32, no. 5, p. 565, 1987.
- [37] H. Gu, B. Yaman, S. Moeller, J. Ellermann, K. Ugurbil, and M. Akçakaya, "Revisiting 1-wavelet compressed-sensing mri in the era of deep learning," *Proceedings of the National Academy of Sciences*, vol. 119, no. 33, p. e2201062119, 2022.